Heat transport imaging in the spin-ladder compound Ca9La5Cu24O41

Otter, M.; Krasnikov, V. V.; Fishman, D. A.; Pshenichnikov, M. S.; Saint-Martin, R.; Revcolevschi, A.; van Loosdrecht, P. H. M.

Published in:
Journal of Magnetism and Magnetic Materials

DOI:
10.1016/j.jmmm.2008.11.075

Publication date:
2009

Journal of Magnetism and Magnetic Materials 321 (2009) 796–799

Contents lists available at ScienceDirect

Journal of Magnetism and Magnetic Materials

journal homepage: www.elsevier.com/locate/jmmm

Heat transport imaging in the spin-ladder compound $Ca_9La_5Cu_{24}O_{41}$

M. Otter [a], V.V. Krasnikov [a], D.A. Fishman [a], M.S. Pshenichnikov [a], R. Saint-Martin [b], A. Revcolevschi [b], P.H.M. van Loosdrecht [a,*]

[a] Zernike Institute for Advanced Materials, Nijenborgh 4, 9747 AG Groningen, The Netherlands
[b] Laboratoire de Chimie des Solides, Universite & Paris-Sud, 91405 Orsay Cedex, France

ARTICLE INFO

Available online 30 November 2008

PACS:
66.30.−h
66.70.Lm
71.27.+a

Keywords:
Thermal transport
Magnon transport
Thermal imaging
Quantum magnet

ABSTRACT

All-optical heat transport imaging on the spin-ladder compound $Ca_9La_5Cu_{24}O_{41}$ is presented. A 'time-of-flight' principle is discussed along with its experimental verification which can be used to measure the bulk thermal diffusion constant. The results of the thermal imaging experiments clearly demonstrate anisotropic magnon heat transport.

1. Introduction

Thermal heat management is one of the most important issues limiting the density and speed of functional elements in electronic devices [1]. Materials with a high room-temperature thermal conductivity usually have the disadvantage that they are electrically conducting (metals), whereas electrical insulators typically have the disadvantage of a low room-temperature thermal conductivity. Recently, it has been shown that low-dimensional quantum magnets might provide an escape route from the seemingly incompatibility of having both a high thermal conductivity and electrically insulating behavior near room temperature [2]. In these materials, the thermal heat current is not carried by phonons or electrons, but rather by quantum spin excitations (called 'magnons' here). The reason that these are so efficient in carrying heat is their strong dispersion (i.e. the high energy per particle), and the fact that spin conservation limits the number of scattering processes leading to long mean paths for the excitations. Current state of the art in thermal conductivity values is about $100\,W\,m^{-1}\,K^{-1}$ at 300 K, and even $140\,W\,m^{-1}\,K^{-1}$ at 175 K, as found in the magnetic ladder compound $Ca_9La_5Cu_{24}O_{41}$ [3]; however, other materials like the magnetic chain compounds $SrCuO_2$ [4] and Sr_2CuO_3 [5] also exhibit unusually large heat conductivity values due to magnon transport. These values are comparable to those found in metals. In addition to the high room-temperature values of heat conductivity, the low-dimensional quantum magnets offer an additional advantage over conventional materials in that the heat conductivity is unidirectional, originating from the highly anisotropic exchange interaction which results in an appreciable dispersion of the magnon-modes in one direction only.

One of the most widely used experiments to determine heat conductivities is the direct heat transport method, where the temperature drop over a sample is measured for a constant heat current (see, for instance, Refs. [2–5]). For actual devices, this might not be the most appropriate method given the small length scale. Therefore, one has to rely on alternative methods to determine the heat conductivity. One attractive method is fluorescent microthermal imaging (FMI) [6] and related techniques. The FMI technique, developed by Kolodner and Tyson [7], is used to measure temperatures of, for example, organic materials, electronics, and gas turbines [8,9]. These all-optical methods make use of the strong temperature dependence of the luminescence in materials such as the rare earth-chelates. The spatial resolution is limited by the wavelength only, making these methods in principle suitable not only for bulk and thin film materials, but also for small devices.

The present work discusses two of these techniques, and provides some preliminary results on the heat transport in a quantum magnet. The first one is a 'time-of-flight' technique, where a heat pulse travels through a sample and is detected on the other side. The second one is a true imaging technique, which maps the two–dimensional (2D) temperature pattern of a sample

* Corresponding author. Tel.: +31 50 363 8149; fax: +31 50 363 4879.
E-mail address: p.h.m.van.loosdrecht@rug.nl (P.H.M. van Loosdrecht).

0304-8853/$ - see front matter © 2008 Elsevier B.V. All rights reserved.
doi:10.1016/j.jmmm.2008.11.075

generated by a small heat spot. The material studied is $Ca_9La_5Cu_{24}O_{41}$, a member of the so-called "telephone number" ladder compounds $(La,Sr,Ca)_{14}Cu_{24}O_{41}$. These orthorhombic compounds contain two quasi-one-dimensional magnetic subsystems along the *c*-axis. The most important one for the present work is the two-legged ladder system with a strong antiferromagnetic Cu–O–Cu exchange interaction between the Cu $S = 1/2$ spins. In addition to these, there are also spin chains between the ladders with a weaker magnetic interaction. Depending on the stoichiometry, these ladders may be hole-doped leading to electrical conductivity in the *c*-direction. The composition $Ca_9La_5Cu_{24}O_{41}$ was chosen to avoid doping in the chains, and hence to avoid any electronic contribution to the heat conductivity. More details on the material and its structure can for instance be found in Refs. [10–12].

2. Sample preparation and coating

Thin platelets (0.8–1 mm) have been cut and polished from single crystals of $Ca_9La_5Cu_{24}O_{41}$ grown by a traveling solvent floating zone method [13]. Following [7], a solution of 1.8 wt% PMMA and 1.2 wt% rare-earth chelate europium thenoyltrifluoroacetonate (EuTTA, Acros Organics) in chlorobenzene was spincoated onto the samples, resulting in a thin (~100 nm) layer of EuTTA/PMMA on one side of the samples.

The TTA molecule absorbs in a wide band around 345 nm. After the energy transfer to the Eu^{3+}-ion, the Eu^{3+}-ion shows emission from its f and d levels, which is strongest at 612 nm (Eu^{3+} 5d level) [14]. The quantum efficiency of this EuTTA layer decreases monotonically with temperature, resulting from a thermal activation of energy transport from the emitting Eu^{3+} 5d level (612 nm) to a nonemitting TTA ligand state [8]. A typical temperature dependence of the phosphorescence (excitation at 370 nm) of a EuTTA/PMMA layer is shown in Fig. 1 for temperatures between 293 and 313 K. The data are plotted as $\ln[I(T = 293+\Delta T)/I(T = 293\,\mathrm{K})]$ versus the temperature raise, ΔT, above room temperature. The sensitivity in this temperature range is found to be about 1.6% K^{-1}.

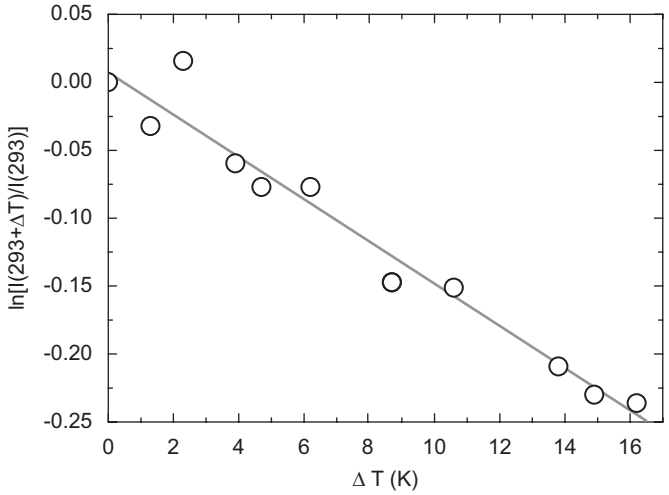

Fig. 1. Calibration curve for the temperature dependence of the phosphorescence for EuTTA. $\Delta T = 0$ corresponds to room temperature (293 K). The excitation wavelength is 370 nm. A temperature difference of 1 K corresponds to a change in the logarithm of the phosphorescence intensity of about 1.6% K^{-1} in this temperature range.

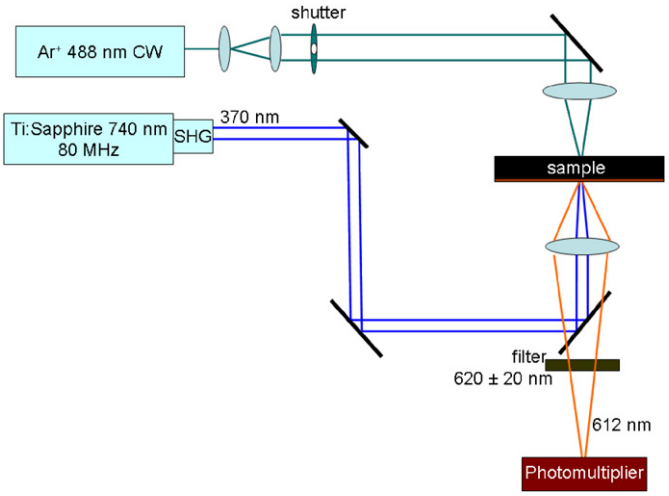

Fig. 2. Schematic representation of the "time-of-flight" setup. An Ar-ion laser (488 nm) is used to excite one side of the sample at a certain time *t*. The time-dependent heat response on the other side of the sample is monitored using the 612 nm emission from a EuTTA/PMMA layer which is continuously excited by the frequency-doubled (370 nm) output of a Ti:Sapphire oscillator.

3. 'Time-of-flight' experiment

The first experiment focuses on measuring the heat diffusivity in the *c*-direction of a 0.8 mm $Ca_9La_5Cu_{24}O_{41}$ crystal platelet, by measuring the time it takes for a heat pulse to travel through the sample. The heat diffusivity is defined as

$$D = \frac{\kappa}{\rho C_p},$$

where κ is the heat conductivity in, ρ is the mass density, and C_p is the specific heat capacity.

The optical scheme of the 'time-of-flight' setup is shown in Fig. 2. An electronically controlled mechanical shutter slices a pulse with duration of ~2 ms out of the output of a 3 W cw Ar-ion laser operation at the wavelength of 488 nm. This provides a heat pulse at the front surface of the sample oriented with the *c*-axis perpendicular to the platelet. A 370 nm quasi cw laser beam (the second harmonic of a Ti:Sapphire laser with ~60 mW averaged power; repetition rate of 80 MHz) was used to excite the phosphorescence of the EuTTA layer, coated on the back side of the sample. The phosphorescence was detected by a photomultiplier tube, digitized and stored in a computer that also controls time synchronization. The temperature raise has been determined using calibration data similar to the one shown in Fig. 1. All measurements were performed at room temperature.

A typical time trace of the response to a 2 ms heating pulse is shown in Fig. 3 (black line). There is a clear delay in the temperature increase measured at the back side of the crystal of about 2 ms. From this one can directly estimate [15] the thermal diffusivity to be ~30 $mm^2\,s^{-1}$.

In the approximation of a short heating pulse the normalized temperature trace may be described by Parker's formula [15]

$$\Delta T(t) = 1 + 2\sum_{m=1}^{\infty}(-1)^m \exp(-m^2\pi^2 Dt/L^2),$$

where D, t and L are the diffusion constant, the time, and the sample thickness, respectively. The time traces have been simulated using Parker's formula convoluted with a 2 ms heating pulse (Fig. 3, grey curve). Although not perfect, the simulations agree reasonably well with the experimental data. The diffusion

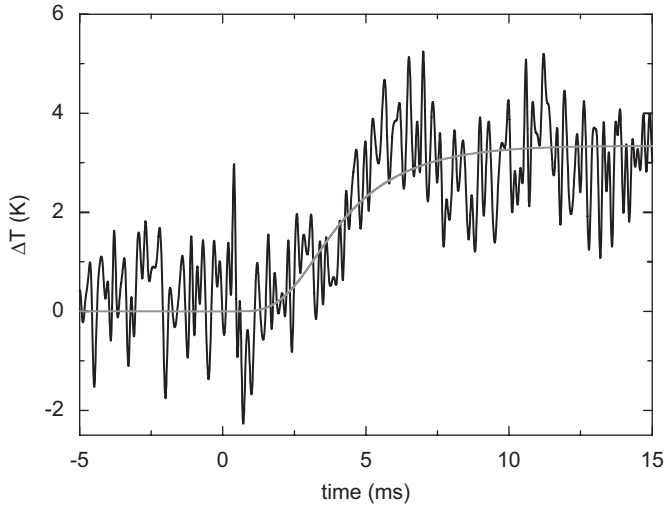

Fig. 3. Temperature rise at the crystal side opposite to the heated side as a function of time (black line). Zero time corresponds to the leading edge of the heat pulse. The grey line gives the best fit to the data of Parker's formula convoluted with the heat pulse.

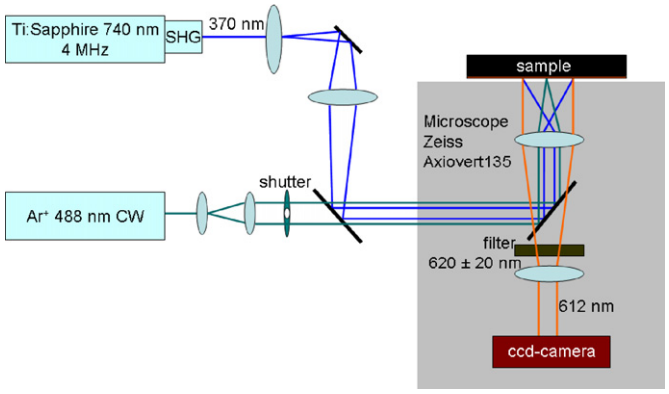

Fig. 4. Schematic drawing of the thermal imaging setup. A focused (spot size of ~5 μm) Ar-ion laser (488 nm) is used as a heat source. The heat response of the sample is monitored using the 612 nm emission from a EuTTA/PMMA layer which is excited by the frequency-doubled (370 nm) output of a Ti:Sapphire oscillator. Timing is controlled through a shutter in the 488 nm beam in combination with a shutter on the CCD camera.

constant D along the c-direction determined in this manner is $30 \pm 5\,\mathrm{mm^2\,s^{-1}}$. This deviates substantially from the diffusivity $D = 150\,\mathrm{mm^2\,s^{-1}}$ calculated from literature data [3]. The most plausible cause of the discrepancy is a limited applicability of Parker's formula. The description neglects in particular the heat diffusion in directions other than perpendicular to the sample surface, which, even though the perpendicular transport should dominate, is not negligible in the present case. In addition, a slight misalignment of the c-axis cannot be excluded. More experiments and numerical simulations of heat transport under our experimental conditions are currently in progress.

4. Fluorescent microthermal imaging

A second technique to study the thermal diffusion in materials is the earlier mentioned FMI, in which the heat pattern on the surface of a sample is imaged using an emission microscopy technique. Although used for crystals here, this method is particularly suited for studies of heat transport in thin films and devices. The optical scheme of the FMI setup is shown in Fig. 4. A focused 488 nm pulse (spot size around 5 μm, power ~10 mW) heats a small volume of the sample. The area around the heat pulse is illuminated by a 370 nm laser pulse (the second harmonic of a Ti:Sapphire, power ~60 mW) to excite the temperature-dependent phosphorescence from the EuTTA/PMMA layer, spin-coated on the crystal surface. The phosphorescence is collected by an objective, filtered from heating/excitation radiations, and imaged onto a Peltier-cooled CCD-camera. The magnification of the objective is 20 times, which for the present system corresponds to a resolution of 0.8 μm per CCD pixel.

Experiments have been performed on two differently oriented crystals: *ac* plane oriented to have the high conductivity c-axis in plane, and *ab* oriented crystals with the c-axis perpendicular to the plane. All measurements were performed at room temperature using a CCD integration time of 40 ms. Obtaining of a thermal

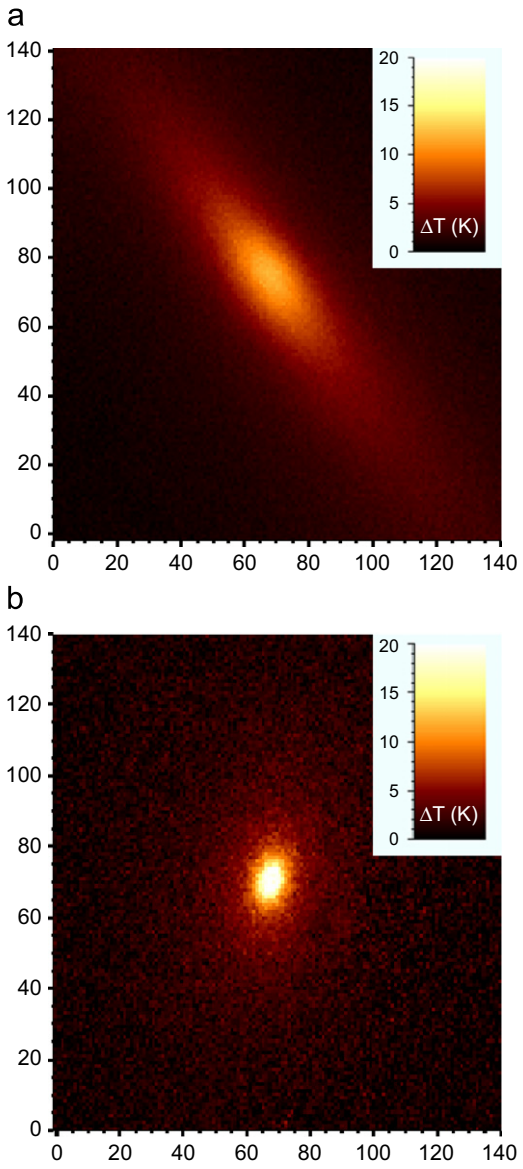

Fig. 5. (a) Thermal image of the *ac*-plane of $La_5Ca_9Cu_{24}O_{41}$ generated by a localized heat pulse in the center of the image. It shows a highly anisotropic pattern due to the high thermal conductivity in the (diagonal) c-direction. (b) Thermal image of the *ab*-plane of $La_5Ca_9Cu_{24}O_{41}$ generated by a localized heat pulse in the center of the image shows an isotropic pattern. The distances on both x- and y-axis are in μm.

image requires recording two subsequent images. First, a "cold" image is acquired with no heating radiation to obtain the emission pattern of the sample at a homogeneous temperature. Then a second image is acquired directly after a 40 ms heat pulse has been applied to the sample. From these images the temperature change is then calculated, using a calibration curve similar to that of Fig. 1.

Fig. 5a shows a thermal heating image obtained on an *ac* oriented sample, i.e. with the *c*-axis in plane (diagonal in this case). The anisotropy of the heat transport is clearly illustrated: the heat pattern forms an elongated elliptical shape, originating from the highly anisotropic heat transport in the *ac* plane. The aspect ratio of the cuts to the 2D phosphorescence intensities along the fast (c) and slow (a) axis is not a constant but varies with the intensity from ~2.3 at 50% of the maximum value to 4 at 20%. In a striking contrast, images obtained on an *ab* oriented crystal under the same experimental conditions (Fig. 5b) yield an isotropic thermal heating image. Its size is similar to that of the short axis of the elliptical pattern of Fig. 5a.

To get a better understanding of the obtained results, we simulated the thermal images by numerically solving the anisotropic three-dimensional heat equation

$$\frac{\partial T}{\partial t} = D_x \frac{\partial^2 T}{\partial x^2} + D_y \frac{\partial^2 T}{\partial y^2} + D_z \frac{\partial^2 T}{\partial z^2},$$

where T is the temperature, and D_α is the diffusion constant in the direction α. A heat pulse, Gaussian-shaped in the space and rectangular in the time domain, was used in the simulations. The penetration depth of the heat was assumed to be 0.002 mm in accordance with the crystal absorption coefficient at 488 nm. The diffusion coefficients D_x, D_y and D_z were calculated from the known thermal conductivity coefficients [3]. The simulated aspect ratio is about 4, which compares favorably to the results obtained experimentally for the ratio far away from the excitation point.

5. Summary

We have shown that fluorescent microthermal imaging is a promising technique to detect and image heat transport in quantum magnets. It is also clear that more effort is needed to derive quantitative values from the experiments. The 'time-of-flight' experiments give a value which is off by a factor of 5 from accepted literature values, and even though the imaging technique does give the correct aspect ratio far away from the heat spot, there are some deviations close to it. Better control of timing in the experiments, improved signal-to-noise ratios and above all more complete theoretical simulations are currently in progress to address these issues. Once established, it is expected that these techniques will prove useful in studies of heat diffusion in thin films and functional devices, as well as in applications involving fast heat transfer processes.

Acknowledgments

We thank S.W. Cheong for the valuable discussion and his suggestion to use EuTTA, and M.T. Lu for his kind help in sample preparations. This work was supported by the FP6-032980-2 NOVMAG project.

References

[1] K. Watari, S.L. Shinde, MRS Bulletin 26 (2001) 440.
[2] A.V. Sologubenko, K. Giannò, H.R. Ott, U. Ammerahl, A. Revcolevschi, Phys. Rev. Lett. 84 (2000) 2714.
[3] C. Hess, C. Baumann, U. Ammerahl, B. Büchner, F. Heidrich-Meisner, W. Brenig, A. Revcolevschi, Phys. Rev. B 64 (2001) 184305.
[4] A.V. Sologubenko, E. Felder, K. Giannò, H.R. Ott, A. Vietkine, A. Revcolevschi, Phys. Rev. B 62 (2000) R6108.
[5] P. Ribeiro, C. Hess, P. Reutler, G. Roth, B. Büchner, J. Magn. Magn. Mater. 290-291 (2005) 334.
[6] D.L. Barton, P. Tangyunyong, Microelectron. Eng. 31 (1996) 271–279.
[7] P. Kolodner, J.A. Tyson, Appl. Phys. Lett. 40 (1982) 782;
P. Kolodner, J.A. Tyson, Appl. Phys. Lett. 42 (1983) 117.
[8] S.W. Allison, G.T. Gillies, Rev. Sci. Instrum. 68 (1997) 2615.
[9] O. Zohar, M. Ikeda, H. Shinagawa, H. Inoue, H. Nakamura, D. Elbaum, D.L. Alkon, T. Yoshioka, Biophys. J. 74 (1998) 82.
[10] E.M. McCarron III, M.A. Subramanian, J.C. Calabrese, R.L. Harlow, Mater. Res. Bull. 23 (1988) 1355;
T. Siegrist, L.F. Schneemeyer, S.A. Sunshine, J.V. Waszczak, R.S. Roth, Mater. Res. Bull. 23 (1988) 1429.
[11] E. Dagotto, T.M. Rice, Science 271 (1996) 618.
[12] M. Matsuda, K. Katsumata, R.S. Eccleston, S. Brehmer, H.J. Mikeska, J. Appl. Phys. 85 (1999) 5642.
[13] U. Ammerahl, G. Dhalenne, A. Revcolevschi, J. Berthon, H. Moudden, J. Cryst. Growth 193 (1998) 55;
U. Ammerahl, A. Revcolevschi, J. Cryst. Growth 197 (1999) 825.
[14] H. Winston, O.J. Marsh, C.K. Suzuki, C.L. Telk, J. Chem. Phys. 39 (1963) 267.
[15] W.J. Parker, R.J. Jenkins, C.P. Butler, G.L. Abbott, J. Appl. Phys. 32 (1961) 1679.